Supplementary information for
Integer topological defects organize stresses driving tissue morphogenesis

Pau Guillamat,[1,*] Carles Blanch-Mercader,[1,2,*]
Guillaume Pernollet,[1] Karsten Kruse,[1,2,3,†] and Aurélien Roux[1,‡]

[1]*Department of Biochemistry, University of Geneva, 1211 Geneva, Switzerland*
[2]*Department of Theoretical Physics, University of Geneva, 1211 Geneva, Switzerland*
[3]*NCCR Chemical Biology, University of Geneva, 1211 Geneva, Switzerland*

Contents

SUPPLEMENTARY VIDEOS LEGENDS

Supplementary Video 1. Unconfined monolayer of C2C12 myoblasts. Phase contrast time-lapse of a proliferating monolayer of myoblasts.

Supplementary Video 2. Spiral-to-aster transition in a C2C12 myoblast disk. Phase contrast time-lapse of myoblast monolayers under circular confinement. In time, cells rearrange from spiral arrangements into aster arrangements.

Supplementary Video 3. Formation of cellular mounds. Phase contrast time-lapse showing the formation of cellular mounds in the center of an aster of myoblasts.

Supplementary Video 4. Cellular spirals. Phase contrast time-lapse of low-density circular islands of myoblasts featuring spiral configurations. Division was blocked with Mitomycin-C.

Supplementary Video 5. Actin dynamics in cellular spirals. Fluorescence confocal time-lapse of the bottom plane of a cellular spiral. Actin was stained with SiR-actin.

Supplementary Video 6. Cellular asters. Phase contrast time-lapse of high-density circular islands of myoblasts. Division was not blocked.

Supplementary Video 7. Actin dynamics in cellular asters. Fluorescence confocal time-lapse of the bottom plane of a cellular aster. Actin was stained with SiR-actin.

Supplementary Video 8. Actin organization and flows in minimal cellular mounds. Z-projection of the top of an actin-labelled mound. Actin was stained with SiR-actin.

Supplementary Video 9. Pillar constriction experiment. Differential interference contrast (DIC) time-lapse showing myoblasts constricting soft hydrogel pillars of different sizes. The consequent pillars' deformation can be observed in the 3D renderings of the pillars obtained from fluorescence images' segmentation.

Supplementary Video 10. Dynamics and collapse of 3D cellular protrusions. Phase contrast time-lapse of a myoblast protrusion, which collapses after confining pattern is degraded.

SUPPLEMENTARY NOTE 1: HYDRODYNAMIC DESCRIPTION OF MONOLAYERS OF ANISOTROPIC CELLS

In this section, we present the phenomenological description of monolayers of elongated cells used in the main text. For details, we refer the reader to Sec. II of Ref. [1].

1.1: Conservation equations

First, we identify the conservation equations characterizing cell monolayers. Let n be the two-dimensional cell number density. Neglecting cell division, growth, and cell death, we write the conservation of mass as

$$\partial_t n + \partial_\gamma (n v_\gamma) = 0, \tag{S1}$$

where γ represents the cartesian coordinates in the substrate plane and $\mathbf{v}$ is the in-plane velocity field. We adopt the Einstein convention such that summation over repeated indices is tacitly assumed. In addition to the cell number density, the state of the monolayer is characterized by the polarization field $\mathbf{p}$, which captures the local average orientation of cellular structures.

Next, we consider momentum conservation. In our experiments, the Reynolds number Re is smaller than one. We thus consider the overdamped limit and the conservation of momentum is expressed through force balance. In our experiments, the lateral extension of C2C12 cells is an order of magnitude larger than its height, 50 μm *vs* 10 μm. We thus consider a thin-film approximation and turn the three-dimensional force balance equation into a two-dimensional description for the height-averaged stress and the height itself [2]. We neglect any fluctuations in the latter, such that force balance is captured by

$$\partial_\beta \sigma^{\mathrm{tot}}_{\alpha\beta} = \xi v_\alpha - T_0 p_\alpha. \tag{S2}$$

Here, $\sigma^{\mathrm{tot}}_{\alpha\beta}$ are the cartesian components of the in-plane total mechanical stress tensor obtained after averaging with respect to the height. The terms on the right hand side of the equation capture external forces resulting from cell-substrate interactions. No net force and torque is applied on the monolayers as a result of these interactions.

The external force density has two components: $\xi\mathbf{v}$ describes friction between the monolayer and the substrate, whereas $T_0\mathbf{p}$ is the traction force of the cells. The friction force depends on the velocity field $\mathbf{v}$. The traction force is independent of the velocity $\mathbf{v}$ and aligned with the polarization field $\mathbf{p}$.

1.2: Constitutive relations

To close the description of monolayers of elongated cells requires constitutive equations. In particular, we need to specify the expressions for the total stress $\sigma^{\rm tot}$ and the time evolution of the polarization field $\mathbf{p}$. To obtain these expressions, we followed the standard approach of non-equilibrium thermodynamics [3] and the procedure is explained in Sec. II B. from Ref. [1].

The total stress tensor $\sigma^{\rm tot}$ is a linear combination of three terms

$$\sigma^{\rm tot}_{\alpha\beta} = \sigma^{\rm s}_{\alpha\beta} + \sigma^{\rm a}_{\alpha\beta} + \sigma^{\rm e}_{\alpha\beta}. \tag{S3}$$

The first term in (S3) corresponds to the symmetric part of the deviatory stress $\sigma^{\rm tot} - \sigma^{\rm e}$ and reads

$$\begin{aligned}\sigma^{s}_{\alpha\beta} = 2\eta\left(v_{\alpha\beta} - \frac{1}{2}v_{\gamma\gamma}\delta_{\alpha\beta}\right) + \bar{\eta}v_{\gamma\gamma}\delta_{\alpha\beta} + \frac{\nu}{2}\left(p_\alpha h_\beta + p_\beta h_\alpha - p_\gamma h_\gamma \delta_{\alpha\beta}\right) + \nu' p_\gamma h_\gamma \delta_{\alpha\beta} \\ - \left(p_\alpha p_\beta - \frac{1}{2}p_\gamma p_\gamma \delta_{\alpha\beta}\right)\zeta\Delta\mu - \delta_{\alpha\beta}\zeta'\Delta\mu - p_\gamma p_\gamma \delta_{\alpha\beta}\zeta''\Delta\mu,\end{aligned} \tag{S4}$$

where $v_{\alpha\beta} = (\partial_\alpha v_\beta + \partial_\beta v_\alpha)/2$ is the symmetric part of the velocity gradient tensor and $\Delta\mu$ the chemical potential difference of ATP and its hydrolysis products, which we consider to be uniform. Furthermore, $\mathbf{h} = -\delta\mathcal{F}/\delta\mathbf{p}$, where $\mathcal{F}$ is the equilibrium free energy. In the context of liquid crystals [8], $\mathbf{h}$ is called the molecular field. It describes the restoring forces associated with deformations of $\mathbf{p}$. The coefficients η, $\bar{\eta}$, ν, ν', ζ, ζ' and ζ'' are phenomenological parameters.

The second term in (S3) corresponds to the antisymmetric part of the deviatory stress and reads

$$\sigma^{a}_{\alpha\beta} = \frac{1}{2}\left(p_\alpha h_\beta - p_\beta h_\alpha\right). \tag{S5}$$

The third term in (S3) corresponds to the Ericksen stress $\sigma^{\rm e}$, which is a generalization of the hydrostatic pressure. For a one-component polar fluid with cell number density n and polarization field $\mathbf{p}$, the general expression for the Ericksen stress tensor reads [4, 5]

$$\sigma^{e}_{\alpha\beta} = (f - n\mu)\delta_{\alpha\beta} - \frac{\partial f}{\partial(\partial_\beta p_\gamma)}\partial_\alpha p_\gamma. \tag{S6}$$

Here, f is the free energy density, such that the free energy $\mathcal{F}$ reads $\mathcal{F} = \int f da$, and $\mu = \frac{\partial f}{\partial n}$ is the chemical potential of the fluid. The Ericksen stress satisfies the Gibbs-Duhem relation [7], which links the intensive variables of the free energy and reads [4, 5]

$$\partial_\gamma \sigma^{e}_{\alpha\gamma} = -n\partial_\alpha\mu - h_\gamma\partial_\alpha p_\gamma. \tag{S7}$$

Next, the time evolution of the polarization field $\mathbf{p}$ is given by the following constitutive equation

$$\partial_t p_\alpha + v_\beta\partial_\beta p_\alpha + \omega_{\alpha\beta}p_\beta = \frac{h_\alpha}{\gamma} - \nu\left(v_{\alpha\beta} - \frac{1}{2}v_{\gamma\gamma}\delta_{\alpha\beta}\right)p_\beta - \nu' v_{\beta\beta}p_\alpha + \lambda\Delta\mu p_\alpha \tag{S8}$$

Here, $\omega_{\alpha\beta} = (\partial_\alpha v_\beta - \partial_\beta v_\alpha)/2$ is the antisymmetric part of the velocity gradient tensor. The coefficients γ, ν, ν', λ are phenomenological parameters.

In Ref. [1], we show that the active isotropic stress proportional to ζ' in (S4) and the term proportional to λ in (S8) amount to a renormalization of parameters aside from possibly introducing additional surface terms. In the following, these terms are omitted.

1.3: Steady state equations in polar coordinates

In order to apply the equations derived in the previous sections to cell monolayers confined to circular domains, in the following, we express them in polar coordinates r and θ. We focus on steady state solutions and assume that they are invariant with respect to rotations around the center of the domain. Finally, we specify the boundary conditions for this situation.

In steady state and assuming rotational invariance, the conservation equation (S1) becomes

$$\partial_r(nv_r) + \frac{nv_r}{r} = 0. \tag{S9}$$

The absence of flows across the domain boundaries, see below, yields $v_r = 0$.

For the polarization field $\mathbf{p}$, we introduce the polar order parameter S and the angle ψ with respect to the radial direction, such that $p_r = S\cos(\psi)$ and $p_\theta = S\sin(\psi)$. In terms of the variables S and ψ, the dynamic equation (S8) for the polarization field in steady state reads

$$\frac{h_\parallel}{\gamma} - \nu S v_{r\theta}\sin(2\psi) = 0 \tag{S10}$$

$$\frac{h_\perp}{\gamma} + S v_{r\theta}\left(1 - \nu\cos(2\psi)\right) = 0. \tag{S11}$$

In these expressions, $h_\parallel = \cos(\psi)h_r + \sin(\psi)h_\theta$ and $h_\perp = -\sin(\psi)h_r + \cos(\psi)h_\theta$ are the components of the field $\mathbf{h}$ parallel and perpendicular to $\mathbf{p}$. Furthermore, $v_{r\theta} = (\partial_r v_\theta - v_\theta/r)/2$ is the off-diagonal component of the symmetric part of the velocity gradient tensor. The components v_{rr} and $v_{\theta\theta}$ vanish at steady state.

Using the variables S and ψ, the components of the deviatory stress can be written as

$$\sigma_{rr,\theta\theta} = \mp\frac{1}{2}S^2\cos(2\psi)\zeta\Delta\mu - S^2\zeta''\Delta\mu \pm \frac{\nu}{2}S\left(h_\parallel\cos(2\psi) - h_\perp\sin(2\psi)\right) + \nu' S h_\parallel \tag{S12}$$

$$\sigma_{r\theta,\theta r} = 2\eta v_{r\theta} - \frac{1}{2}S^2\sin(2\psi)\zeta\Delta\mu + \frac{\nu}{2}S\left(h_\parallel\sin(2\psi) + h_\perp\cos(2\psi)\right) \pm \frac{S h_\perp}{2}, \tag{S13}$$

where the upper (lower) signs correspond to the first (second) index pair. The force balance

equation (S2) takes the form

$$\partial_r \sigma^{\rm tot}_{rr} + \frac{\sigma^{\rm tot}_{rr} - \sigma^{\rm tot}_{\theta\theta}}{r} = -T_0 S\cos(\psi) \tag{S14}$$

$$\partial_r \sigma^{\rm tot}_{\theta r} + \frac{\sigma^{\rm tot}_{\theta r} + \sigma^{\rm tot}_{r\theta}}{r} = \xi v_\theta - T_0 S\sin(\psi). \tag{S15}$$

By employing the Gibbs-Duhem relation (S17), which in polar coordinates and considering rotational invariance reads

$$\partial_r \sigma^{e}_{rr} + \frac{\sigma^{e}_{rr} - \sigma^{e}_{\theta\theta}}{r} = -n\partial_r\mu - h_r\partial_r p_r - h_\theta \partial_r p_\theta = -n\partial_r\mu - h_\parallel \partial_r S - h_\perp S\partial_r\psi \tag{S16}$$

$$\partial_r \sigma^{e}_{\theta r} + \frac{\sigma^{e}_{r\theta} + \sigma^{e}_{\theta r}}{r} = -h_r(\frac{-p_\theta}{r}) - h_\theta(\frac{p_r}{r}) = -\frac{h_\perp S}{r}, \tag{S17}$$

we can furthermore eliminate the Ericksen stress in Eq. (S15) and obtain

$$\partial_r \sigma_{\theta r} + \frac{2\sigma_{\theta r}}{r} = \xi v_\theta - T_0 S\sin(\psi). \tag{S18}$$

The expressions for the Ericksen stress σ^e and the molecular field $\mathbf{h}$ are given in the Supplementary notes 1.5 and 1.6. In the case of small confinement, our experiments show a disordered region in the center and orientational order close to the boundary. We choose a corresponding free energy, where the ground state is isotropic and to boundary conditions that impose orientational order. We study this case in Supplementary notes 2 and 4 and the corresponding free energy is given in Supplementary note 1.5. In Supplementary note 8 we study the case of a topological defect in large confinement. In this case we consider that the system develops spontaneous orientational order and employ the free energy given in Supplementary note 1.6. Such a situation can be observed in extended confluent layers of C2C12 cells, which generate spontaneous long-range nematic order [6]. For more details on the liquid crystal properties of monolayers of elongated cells see Ref. [1].

1.4: Boundary conditions in a circular domain

It remains to fix the conditions on the fields at the boundary of the circular domain at $r = R$, where R is its radius. Compatible with our experiments, we impose that there is no flux of material into the domain at the boundary. At the same time, there is no tangential force applied to the cell monolayer at the edge of the domain. For the boundary conditions on the polarization field, let us first note that the polar order parameter is maximal at the boundary. Without loss of generality, we fix this value to be one. Furthermore we impose that there are no gradients in ψ at the boundary. In summary, we thus have

$$(S, \partial_r\psi, \sigma^{\rm tot}_{\theta r}, v_r)|_{r=R} = (1, 0, 0, 0) \tag{S19}$$

Note that the total cell number is conserved and thus a parameter of our system.

In our experiments, the monolayers are disordered in the center of the domains, and we impose $S = 0$ at $r = 0$. Due to our assumption of rotational invariance, we also need to impose regularity of the solutions at $r = 0$. In total we have

$$(S, \partial_r\psi, v_\theta, v_r)|_{r=0} = (0, 0, 0, 0) \tag{S20}$$

1.5: Ericksen stress and molecular field for a liquid crystal with an isotropic ground state

In this subsection, we compute for a compressible polar liquid crystal the Ericksen stress tensor σ^e and the molecular fields $\mathbf{h}$. We consider the free energy

$$\mathcal{F} = \int_{\mathcal{A}} \left\{ \frac{B}{2}\left(1 - \frac{n}{n_0}\right)^2 + \frac{\chi}{2}p_\alpha^2 + \frac{\mathcal{K}}{2}(\partial_\alpha p_\beta)^2 \right\} da. \tag{S21}$$

For a system with cell number density n and polarization field $\mathbf{p}$, the general expression for the Ericksen stress tensor is given by Eq. (S6). For the free energy (S21), we obtain

$$\sigma^e_{\alpha\beta} = \left[\frac{B}{2}\left(1 - \frac{n^2}{n_0^2}\right) + \frac{\chi}{2}p_\gamma^2 + \frac{\mathcal{K}}{2}(\partial_\gamma p_\delta)^2\right]\delta_{\alpha\beta} - \mathcal{K}(\partial_\alpha p_\gamma)(\partial_\beta p_\gamma). \tag{S22}$$

Writing the radial and the azimuthal components of the polarization vector as $p_r = S\cos(\psi)$ and $p_\theta = S\sin(\psi)$, respectively, the components of the Ericksen stress in polar coordinates are

$$\sigma^e_{rr} = \frac{B}{2}\left(1 - \frac{n^2}{n_0^2}\right) + \frac{\chi}{2}S^2 + \frac{\mathcal{K}}{2}\left[\frac{S^2}{r^2} - (\partial_r S)^2 - S^2(\partial_r\psi)^2\right] \tag{S23}$$

$$\sigma^e_{r\theta} = \sigma^e_{\theta r} = -\mathcal{K}S^2\frac{\partial_r\psi}{r} \tag{S24}$$

$$\sigma^e_{\theta\theta} = \frac{B}{2}\left(1 - \frac{n^2}{n_0^2}\right) + \frac{\chi}{2}S^2 - \frac{\mathcal{K}}{2}\left[\frac{S^2}{r^2} - (\partial_r S)^2 - S^2(\partial_r\psi)^2\right], \tag{S25}$$

where we have assumed rotational invariance.

Assuming rotational invariance, the free energy (S21) can be written as

$$\mathcal{F} = 2\pi\int_{\mathcal{A}} \left\{ \frac{B}{2}\left(\frac{n}{n_0} - 1\right)^2 + \frac{\chi}{2}(p_r^2 + p_\theta^2) + \frac{\mathcal{K}}{2}\left[(\partial_r p_r)^2 + (\partial_r p_\theta)^2 + \frac{p_r^2}{r^2} + \frac{p_\theta^2}{r^2}\right] \right\} r dr. \tag{S26}$$

From this expression, we obtain the components of the molecular field as

$$h_r = -\frac{\delta\mathcal{F}}{\delta p_r} = -\chi p_r + \mathcal{K}\left[\frac{1}{r}\partial_r(r\partial_r p_r) - \frac{p_r}{r^2}\right] \tag{S27}$$

$$h_\theta = -\frac{\delta\mathcal{F}}{\delta p_\theta} = -\chi p_\theta + \mathcal{K}\left[\frac{1}{r}\partial_r(r\partial_r p_\theta) - \frac{p_\theta}{r^2}\right]. \tag{S28}$$

After expressing the radial and azimuthal components of the polarization field as $p_r = S\cos(\psi)$ and $p_\theta = S\sin(\psi)$, the components of the molecular field parallel and perpendicular to the polarization field, $h_\parallel = \cos(\psi)h_r + \sin(\psi)h_\theta$ and $h_\perp = -\sin(\psi)h_r + \cos(\psi)h_\theta$, read

$$h_\parallel = -\chi S + \mathcal{K}\left[\partial_{rr}S + \frac{\partial_r S}{r} - \frac{S}{r^2} - S(\partial_r\psi)^2\right] \tag{S29}$$

$$h_\perp = \mathcal{K}\left[S\partial_{rr}\psi + \frac{S\partial_r\psi}{r} + 2(\partial_r S)(\partial_r\psi)\right]. \tag{S30}$$

The Gibbs-Duhem relation (S7) can be verified explicitly by using expressions (S23)-(S25) for the components of the Ericksen stress and (S29) and (S30) for $h_\parallel$ and $h_\perp$.

1.6: Ericksen stress and molecular field for a liquid crystal with an ordered ground state

In this subsection, we compute the Ericksen stress tensor σ^e and the molecular field $\mathbf{h}$ for a compressible liquid crystal that exhibits orientational order at equilibrium. We consider the free energy

$$\mathcal{F} = \int_{\mathcal{A}} \left\{ \frac{B}{2}\left(1 - \frac{n}{n_0}\right)^2 - \frac{\chi_2}{2}p_\alpha^2 + \frac{\chi_4}{4}p_\alpha^4 + \frac{\mathcal{K}}{2}(\partial_\alpha p_\beta)^2 \right\} da. \tag{S31}$$

For a system with cell number density n and polarization field $\mathbf{p}$, the general expression for the Ericksen stress tensor is given by Eq. (S6). With the free energy (S31), we obtain

$$\sigma^e_{\alpha\beta} = \left[\frac{B}{2}\left(1 - \frac{n^2}{n_0^2}\right) - \frac{\chi_2}{2}p_\gamma^2 + \frac{\chi_4}{4}p_\gamma^4 + \frac{\mathcal{K}}{2}(\partial_\gamma p_\delta)^2\right]\delta_{\alpha\beta} - \mathcal{K}(\partial_\alpha p_\gamma)(\partial_\beta p_\gamma). \tag{S32}$$

Writing the radial and the azimuthal components of the polarization vector as $p_r = S\cos(\psi)$ and $p_\theta = S\sin(\psi)$, respectively, the components of the Ericksen stress in polar coordinates are

$$\sigma^e_{rr} = \frac{B}{2}\left(1 - \frac{n^2}{n_0^2}\right) - \frac{\chi_2}{2}S^2 + \frac{\chi_4}{4}S^4 + \frac{\mathcal{K}}{2}\left[\frac{S^2}{r^2} - (\partial_r S)^2 - S^2(\partial_r\psi)^2\right] \tag{S33}$$

$$\sigma^e_{r\theta} = \sigma^e_{\theta r} = -\mathcal{K}S^2\frac{\partial_r\psi}{r} \tag{S34}$$

$$\sigma^e_{\theta\theta} = \frac{B}{2}\left(1 - \frac{n^2}{n_0^2}\right) - \frac{\chi_2}{2}S^2 + \frac{\chi_4}{4}S^4 - \frac{\mathcal{K}}{2}\left[\frac{S^2}{r^2} - (\partial_r S)^2 - S^2(\partial_r\psi)^2\right], \tag{S35}$$

where we have assumed rotational invariance.

Assuming rotational invariance of our system, the free energy (S31) can be written as

$$\mathcal{F} = 2\pi\int_{\mathcal{A}} \left\{ \frac{B}{2}\left(\frac{n}{n_0} - 1\right)^2 - \frac{\chi_2}{2}(p_r^2 + p_\theta^2) + \frac{\chi_4}{4}(p_r^2 + p_\theta^2)^2 + \frac{\mathcal{K}}{2}\left[(\partial_r p_r)^2 + (\partial_r p_\theta)^2 + \frac{p_r^2}{r^2} + \frac{p_\theta^2}{r^2}\right] \right\} r dr. \tag{S36}$$

From this expression, we obtain the components of the molecular field as

$$h_r = -\frac{\delta \mathcal{F}}{\delta p_r} = \chi_2 p_r - \chi_4 (p_r^2 + p_\theta^2) p_r + \mathcal{K}\left[\frac{1}{r}\partial_r(r\partial_r p_r) - \frac{p_r}{r^2}\right] \tag{S37}$$

$$h_\theta = -\frac{\delta \mathcal{F}}{\delta p_\theta} = \chi_2 p_\theta - \chi_4 (p_r^2 + p_\theta^2) p_\theta + \mathcal{K}\left[\frac{1}{r}\partial_r(r\partial_r p_\theta) - \frac{p_\theta}{r^2}\right]. \tag{S38}$$

After expressing the radial and azimuthal components of the polarization field as $p_r = S\cos(\psi)$ and $p_\theta = S\sin(\psi)$, the components of the molecular field parallel and perpendicular to the polarization field, $h_\parallel = \cos(\psi)h_r + \sin(\psi)h_\theta$ and $h_\perp = -\sin(\psi)h_r + \cos(\psi)h_\theta$, read

$$h_\parallel = \chi_2 S - \chi_4 S^3 + \mathcal{K}\left[\partial_{rr} S + \frac{\partial_r S}{r} - \frac{S}{r^2} - S(\partial_r \psi)^2\right] \tag{S39}$$

$$h_\perp = \mathcal{K}\left[S\partial_{rr}\psi + \frac{S\partial_r \psi}{r} + 2(\partial_r S)(\partial_r \psi)\right]. \tag{S40}$$

The Gibbs-Duhem relation (S7) can be verified explicitly by using expressions (S33)-(S35) for the components of the Ericksen stress and (S39) and (S40) for $h_\parallel$ and $h_\perp$.

SUPPLEMENTARY NOTE 2: STEADY STATE MECHANICS OF ASTERS AND SPIRALS

In this section, we discuss steady state mechanical patterns generated by integer topological defects from the theoretical description presented in Supplementary note 1. In particular, we focus on the velocity and orientational order patterns in spirals as well as the active force density, stress and cell number density patterns in asters, which are presented in Fig. 4 of the main text. In this section, we use the free-energy density f described in Supplementary note 1.5. For more details on the subsequent analysis, we refer to Ref. [1].

To obtain the orientational order and velocity patterns from Fig. 4B-C of the main text, we use the following procedure. Spirals with a uniform angle of the polarization field $\psi = \psi_0$ that satisfy the condition $\nu \cos 2\psi_0 = 1$ are solutions of Eq. (S11) with the boundary conditions (S19) and (S20). Real solutions for ψ_0 only exist for $|\nu| \geq 1$. The profiles of the polar order parameter S and azimuthal velocity v_θ were obtained by solving numerically Eqs. (S10) and (S18) with the boundary conditions (S19) and (S20). The theoretical curves presented in Fig. 4B-C of the main text are fits to the experimental data. The fitting procedure is explained in Section VIB in Ref. [1].

To obtain the active force density patterns shown in Fig. 4F of the main text, we use the following procedure. First, we define the active force surface density as

$$\mathbf{f}^{a,s} = T_0 \mathbf{p} + \nabla \cdot \sigma^{\mathrm{act}}, \tag{S41}$$

and the active force line density at the boundary of the circular domain as

$$\mathbf{f}^{a,l} = -\sigma^{\mathrm{act}} \cdot \hat{\mathbf{r}}|_{r=R}. \tag{S42}$$

Here, the active stress σ^{act} corresponds to the terms in the total stress tensor associated with active processes. It reads

$$\sigma^{\mathrm{act}}_{\alpha\beta} = -\zeta\Delta\mu(p_\alpha p_\beta - \frac{1}{2}p_\gamma p_\gamma \delta_{\alpha\beta}) - \zeta''\Delta\mu p_\gamma p_\gamma \delta_{\alpha\beta}. \tag{S43}$$

In Fig. 4F of the main text, the magenta arrows correspond to the normalised surface active force density (S41) and the green arrows to the normalised line active force density at the boundary (S42).

We obtained the stress and cell number density patterns shown in Fig. 4E and G of the main text by fitting theoretical curves to experimental data. The analysis is restricted to a parameter regime where the contribution from active anisotropic stresses dominate that of traction forces. The theoretical fits in Fig. 4E and G of the main text have been obtained in the limit of small confinement, such that $R \ll \sqrt{\mathcal{K}/\chi}$, where $\mathcal{K}$ and χ are elastic parameters of the free-energy density (S21). In this limit, the cell number density and stress profiles are parabolic.

SUPPLEMENTARY NOTE 3: STEADY STATE MECHANICAL PATTERNS DRIVEN BY INTERFACIAL EFFECTS

In this section, we study the effects of imposing a tangential velocity at the boundary of the confinement region. We show that such interfacial effects are not sufficient to account for our experimental data. To this end, we discuss the steady state solutions when the orientational order is absent and the system is only driven by interfacial effects. After presenting the steady state solutions, we compare them to a monolayer of C2C12 myoblasts confined to a circular domain.

In absence of orientational order, $S = 0$ in the expressions presented in Supplementary note 1. In this case, the systems lacks an internal driving because the active processes are proportional to the polar order parameters S. Instead we consider the system to be driven at the boundary. Specifically, we fix the azimuthal velocity of the cell monolayer at the edge of the domain, $v_\theta|_{r=R} = v^0_\theta$. We keep the remaining boundary conditions given in Eq. (S19).

The components of the total stress can now be obtained from the components of the deviatory stress (S12) and (S13) and the components of the Ericksen stress (S23) and (S24). The total stress

reads in this case

$$\sigma^{\rm tot}_{rr,\theta\theta} = \frac{B}{2}\left(1 - \frac{n^2}{n_0^2}\right) \tag{S44}$$

$$\sigma^{\rm tot}_{r\theta,\theta r} = 2\eta v_{r\theta} \equiv \eta(\partial_r v_\theta - v_\theta/r). \tag{S45}$$

By inserting these into the force balance equations (S14) and (S18) and enforcing the boundary conditions (S19) and (S20), we obtain the azimuthal velocity field v_θ and cell number density n

$$v_\theta = v_\theta^0 \frac{I_1(r\sqrt{\xi/\eta})}{I_1(R\sqrt{\xi/\eta})} \tag{S46}$$

$$n = n^{\rm tot}, \tag{S47}$$

where the total cell number density is $n^{\rm tot}\pi R^2$ and I_α denotes the modified Bessel function of the first kind. The solutions for the total stress are

$$\sigma^{\rm tot}_{rr,\theta\theta} = \frac{B}{2}\left(1 - \frac{(n^{\rm tot})^2}{n_0^2}\right) \tag{S48}$$

$$\sigma^{\rm tot}_{r\theta,\theta r} = \sigma^0_{\theta r} I_2(r\sqrt{\xi/\eta}), \tag{S49}$$

where $\sigma^0_{\theta r}$ is a function of v^0_θ, the geometrical parameter R, and the material parameters η and ξ. For an aster, we take $v^0_\theta = \sigma^0_{\theta r} = 0$.

As explained in [1], in our experiments, we used circular elastic pillars placed in the center of the circular domain to measure the force exerted by the cell monolayer. Neglecting deviations from the profiles calculated above that are caused by the finite diameter of the pillar, this force is

$$\mathbf{f}_i = \sigma^{\rm tot}(r) \cdot \hat{\mathbf{r}}, \tag{S50}$$

Although this expression is correct only in the limit, where the diameter of the pillars tends to zero, it gives an approximate value for pillars with finite diameter. For an aster, we find

$$\mathbf{f}_i = \frac{B}{2}\left(1 - \frac{(n^{\rm tot})^2}{n_0^2}\right)\hat{\mathbf{r}} = f_0\hat{\mathbf{r}}. \tag{S51}$$

Next, we compare these profiles to our experimental data. Specifically, we used the azimuthal velocity in spirals on islands with radius $R = 50$ μm, 100 μm and 150 μm, as well as, the cell number density and stress patterns in asters on islands with radius 100 μm. In the first set of experiments, spirals were treated with 10 μM mitomycin-C. To quantify the difference between the experiments and the theoretical profiles, for each experimental condition we used the following error function

$$\mathcal{E} = \sum |Y^t(r_i) - Y^e(r_i)|\Delta r_i, \tag{S52}$$

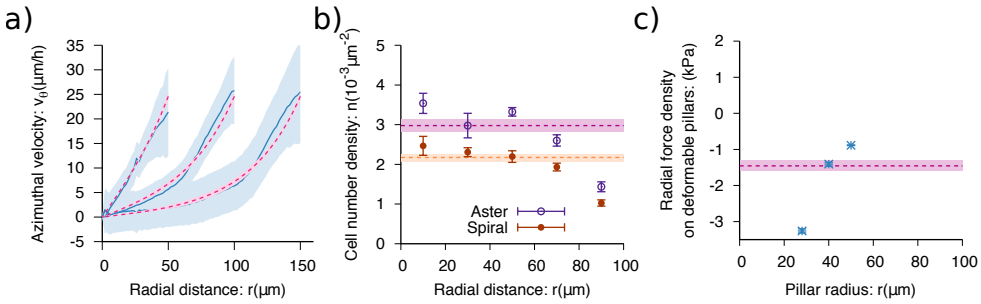

Supplementary figure 1: Theoretical fits to experimental data. a) Azimuthal velocity v_θ as a function of the radial coordinate r. Profiles for three different confinement radii $R = 50$ μm, 100 μm and 150 μm are shown (N=11, 12 and 5, respectivelly). Dashed magenta curves: best theoretical fits given by Eq. (S46). Solid blue curves: averaged experimental curves. b) Cell number density. Filled dark orange circles: experimental data for spirals at day 1 after confluence (N=10). Empty purple circles: experimental data for asters at day 3 after confluence (N=9). Light purple and light orange dashed curves correspond to theoretical fits of Eq. (S47) for asters and spirals, respectively. c) Radial force density on deformable pillar as a function of the pillar's radius r. Blue crosses: experimental data at day 1 after confluence. Light purple dashed curves correspond to theoretical fits of Eq. (S51). Error bars in theoretical fits correspond to the standard deviation of parameter values that lead to $\mathcal{E} < 1.1\mathcal{E}_{min}$. Experimental data are presented as mean values +/- SE.

where Y represents a physical variable, such as n, $\mathbf{f}_i \cdot \hat{\mathbf{r}}$ or v_θ. Here, the superscript t stands for theoretical and e for experimental. The sum runs over the radial positions at which the observable Y^e was measured. The difference between sample points $\Delta r_i = r_{i+1} - r_i$ is related to the experimental resolution, which is typically of the order of 5 μm. To compute the error (S52) for the azimuthal velocity profiles in spirals, we sum the error function for each of the three experimental islands with radius $R = 50$ μm, 100 μm and 150 μm and normalise each error function by the number of data points for each condition. We analysed separately the error function (S52) for the cell number density and stress patterns in asters on islands with radius 100 μm. For each experimental condition, there is a parameter set that gives an absolute minimum for each of the previous error functions $\mathcal{E} = \mathcal{E}_{min}$. The error bars were computed as the standard deviation of the parameter sets with $\mathcal{E} < 1.1\mathcal{E}_{min}$.

Supplementary figure 1 shows the comparison between the theoretical profiles and the experimental data, and the material parameters that were obtained are summarized in Supplementary table 1. We found a parameter set that provides a good fit to the azimuthal velocity profiles for varying confinement radii, Supplementary figure 1a, which provided the parameter values for the velocity scale v_θ^0 and $\sqrt{\eta/\xi}$ in Supplementary table 1. This shows that the velocity patterns in

spirals are compatible with a description of a compressible fluid driven by interfacial effects. In contrast, the experimental cell density profiles for both asters and spirals decrease as a function of the radial coordinate r, whereas the theoretical profiles (S47) are uniform, Supplementary figure 1b. Similarly, the radial force density on elastic pillars near the center $\mathbf{f}_i \cdot \hat{\mathbf{r}}$ increased with the radius of the pillar, whereas the theoretical predictions (S51) are uniform, Supplementary figure 1c. This analysis shows that our experimental data are not captured by an active fluid without orientational order and driven by interfacial effects.

$v_\theta^0(\mu m/h)$	$\sqrt{\eta/\xi}(\mu m)$	$n^{\mathrm{tot}}(10^{-3}\mu m^{-2})$	$f_0(kPa)$
25 ± 1	37 ± 4	3.0 ± 0.2	-1.5 ± 0.1

Supplementary table 1: Table of material parameters for a compressible fluid driven by interfacial effects. The value of n^{tot} corresponds to the fit for asters. Error bars correspond to std of all parameter value with $\mathcal{E} < 1.1\mathcal{E}_{min}$.

SUPPLEMENTARY NOTE 4: COMPARISON BETWEEN THE MECHANICAL STRESS PATTERNS OF ASTERS AND SPIRALS AT STEADY STATE

In this section, we compare the steady state stress patterns generated by integer topological defects in the limit of small confining domains. In addition, we use these results to interpret the growth of multicellular protrusions in C2C12 assemblies confined to circular domains, where we observed structures presenting spirals and asters.

We use the free-energy density (S21), such that orientational order is induced by the boundary and focus on the case, where R is smaller than the penetration length of the orientational order $\sqrt{\mathcal{K}/\chi}$. Here $\mathcal{K}$ and χ are elastic parameters of the free-energy density (S21). For $|\gamma\nu\sin(2\psi)v_{r\theta}| \ll \chi$, the steady state profiles for the polar order parameter are well-approximated by $S = r/R$. This result is exact for asters, $\psi_0 = 0$. The value of ψ_0 in spirals is set by the condition $\nu\cos(2\psi_0) = 1$ from Eq. (S11), which needs $|\nu| \geq 1$ for a real solution to exist.

To quantify stress in the system, we use the trace of the total stress tensor and define

$$\sigma = \frac{\sigma_{rr} + \sigma_{\theta\theta}}{2} \approx -S^2\zeta''\Delta\mu + \frac{B}{2}\left(1 - \frac{n^2}{n_0^2}\right) + \frac{\chi}{2}S^2. \tag{S53}$$

Because the profiles of the polar order parameter S are the same for asters and spirals, the difference

in the stress σ between them takes the form

$$\sigma_A - \sigma_S = \frac{B}{2n_0^2}\left(n_S^2 - n_A^2\right), \tag{S54}$$

where the subscript A stands for aster and the subscript S for spirals. Considering that the cell number density variations are small compared to the reference density n_0 and that the total cell number density is the same for asters and spirals, we can use Eqs. (32) and (60) from Ref. [1] and recast Eq. (S54) into

$$\sigma_A - \sigma_S \approx \left(\frac{T_0 R}{2}(\cos(\psi_0) - 1) - \zeta\Delta\mu(\cos(2\psi_0) - 1)\right)\left(\frac{r^2}{R^2} - \frac{1}{2}\right). \tag{S55}$$

The stress difference $\sigma_A - \sigma_S$ between asters and spirals depend on two different active processes: traction forces proportional to T_0 and gradients of anisotropic active stresses proportional to $\zeta\Delta\mu$, but not on the gradients of isotropic active stresses proportional to $\zeta''\Delta\mu$. Supplementary figure 2a-b shows $\sigma_A - \sigma_S$ (S55) for varying values of the spiral angle ψ_0 and for each of the active processes.

Let us use the above results to interpret the growth of multicellular protrusions in C2C12 assemblies confined to small circular domains. The orientational order corresponds to an aster at the base of such a protrusion and transits to a spiral as the distance to the base increases. We can qualitatively discuss the stress along the axis of the protrusion by considering a planar spiral on top of a planar aster, see Supplementary figure 2c. In Ref. [1], we concluded that the mechanics of asters and spirals showed that active anisotropic stresses are predominant in C2C12 monolayers in small circular domains. In this case, $\sigma_A < \sigma_S$ near the center of the circular domains and $\sigma_A > \sigma_S$ near the boundary, Supplementary figure 2b. This suggests that the stress σ increases from the base to the top near the geometrical center of the system and decreases from the base to the top at the outer interface. Such a stress gradient pattern could drive vortical flows in the direction perpendicular to the substrate plane, such that cells flow upwards in the center and downwards at the surface of the protrusion.

SUPPLEMENTARY NOTE 5: FABRICATION OF PEG HYDROGEL DISKS AND MEASUREMENT OF THEIR ELASTIC PROPERTIES

To characterize the elastic modulus of the PEG hydrogels we prepared 300 μm-high disks of 4arm-PEG (MW 20,000) with different densities (20, 10, 5 and 2.5%w/v). In order to prepare the disks, we added photopolymerizable solution (described in Methods) in circular PMDS wells (14 mm diameter, 300 μm high) placed onto plasma-treated glass-bottom dishes (Mattek). We

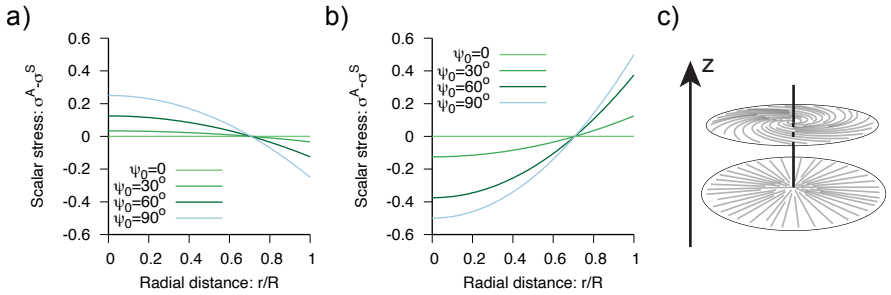

Supplementary figure 2: Difference in the trace of the total stress tensor between asters and spirals. a, b) Difference of the stress $\sigma_A - \sigma_S$ between asters and spirals as a function of the radial coordinate (S55) and for varying values of ψ_0 as indicated in the legend. a) Dominant active processes generate traction forces and the stress scale is $T_0 R$. b) Dominant active processes generate anisotropic active stress and the stress scale is $\zeta \Delta\mu$. The radius of the circular domain is R. c) Schematic of the orientational order in a multicellular protrusion. An aster at the base $z = 0$, which is poised below a spiral. Both defects are aligned in the z direction.

then covered the wells with a glass coverslip. Subsequently, we polymerized the whole content of the wells by illuminating the samples 1 min in a UV-curing chamber (375 nm, Asiga Flash), obtaining hydrogel disks 14 mm in diameter and 1 mm in height. After polymerization, gels were rinsed with double-distilled water and kept under water at 4°C.

Force-displacement curves were obtained by using a FT-S100 micro-force sensing spherical probe (r = 250 μm, Femtotools). We performed 9 indentations for each gel at 2 μm/s and obtained Force vs Displacement curves (Supplementary figure 3a,b). Calibration hydrogels (4 and 50 kPa, Petrisoft) were employed to complete the measurements. The elastic modulus of the lowest density gel (2.5%) was $\sim$ 4 kPa (Supplementary figure 3c).

SUPPLEMENTARY NOTE 6: COMPRESSIVE BEHAVIOR OF CELLULAR MOUNDS AND RINGS

The use of pillars for monitoring compressive stresses within cellular mounds may promote the formation of actin/multicellular rings, thus leading to defect-independent stresses.

Indeed, whereas the orientation and velocity fields at the periphery of the confinement in the presence of pillars were similar to those for asters in the absence of pillars (Extended Data Fig. 6), cells near the pillar surface appeared aligned with the pillar walls (Extended Data Fig. 7). To test the contribution of multicellular rings to pillar compression, mounds around pillars were treated with the ROCK inhibitor Y-27632. From the pillar volume difference before and after treatment,

we observed a reduction of the compressive stress of $0.87 \pm 0.04\ kPa$ (N=23) (Fig. 5E). Importantly, pillars in mounds often did not completely relax after Y-27632 treatment (Fig. 5D,left), showing the existence of residual compressive stresses within the cell monolayers.

Finally, we plated cells on low-adhesion ring micro-patterns, which formed multicellular rings around pillars (Fig. 5D,right). Also, in this condition, we observed compression of the pillars and inferred a stress of 0.35 ± 0.08 kPa (N=5) (Fig. 5E), lower than for cellular mounds. This result shows that distal cells, forming spirals and asters in mounds, contributed to the generation of the compressive stresses. Differently from cellular mounds, pillars surrounded by multicellular rings completely relaxed after application of Y-27632 (Fig. 5D,right). Altogether, these results evidence the existence of defect-mediated stresses in multicellular mounds that are independent from actomyosin or multicellular rings.

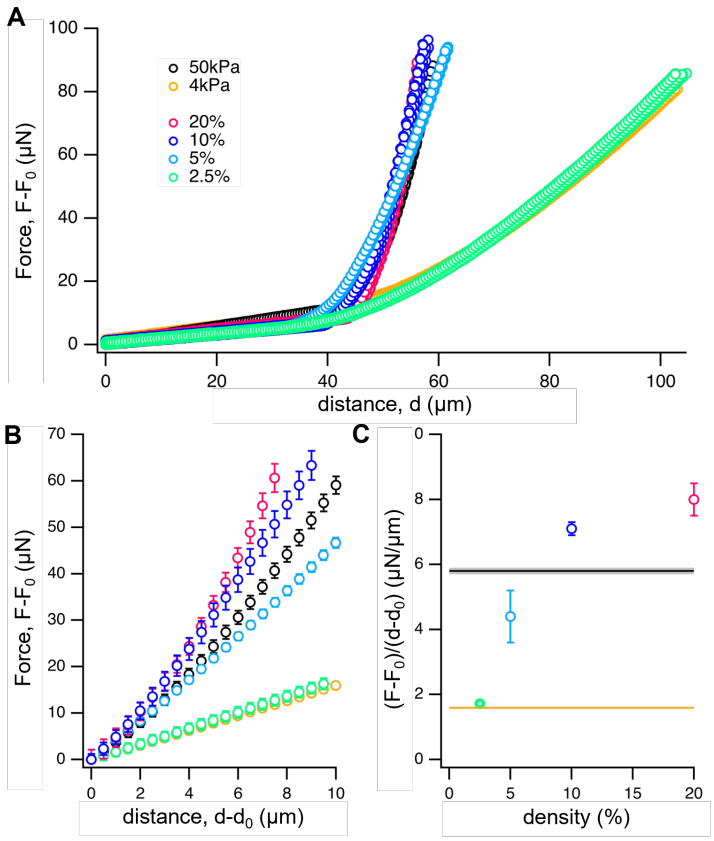

Supplementary figure 3: Mechanical characterization of PEG hydrogels. a) Force-displacement curves ($N = 9$) for gels of different densities and calibration gels with $E = 4$ and 50 kPa. b) Averaged curves from a (N=9). Data is normalized by the distance at which indentation starts (d_0, inflection points in a). F_0 corresponds to the force at d_0. c) Average slopes from curves in b obtained by linear fits and prior to averaging (N=9 indentations per composition). Data are presented as mean values ± SD.

SUPPLEMENTARY NOTE 7: DEFLECTION OF ELASTIC PILLARS

In this section, we discuss some characteristics of the force patterns in cellular mounds by analyzing the deformation of elastic pillars that are clamped away from the geometrical center of the circular domains, see Fig. 5 in the main text. Specifically, we apply the theory of slender elastic rods and small deflections to interpret the experimental data.

We describe the elastic pillar as a slender rod of length L and with a circular cross-section of radius δ. As shown in Supplementary figure 4a, we consider that the bending deformation of the rod takes place in the $x-z$ plane, with z being the direction perpendicular to the substrate plane and x the direction parallel to the substrate plane that connects the center of the circular domain with the center of the elastic pillar. The center line of the rod can be parametrized as $\mathbf{r}(z) = (x(z), 0, z)$. The end of the rod in contact with the substrate is at the position $\mathbf{r}(z=0) = (x(0), 0, 0)$, where $x(0) = x_0$, and the other end of the rod is at position $\mathbf{r}(z=L) = (x(z=L), 0, L)$.

The mechanical interactions between cells from the multicellular mounds and the elastic pillar are described as an external force density $\mathbf{K}$, Supplementary figure 4a. This force per unit length may depend on the specific details of the interactions at the cell-pillar interface and the material properties of the mound. As we motivate below, Supplementary note 7.1, we approximate the external force density generated by the multicellular mounds on the elastic pillars by

$$\mathbf{K} = (-k_o x(z), 0, 0), \tag{S56}$$

where k_o is an effective parameter that depends on the material of the cellular mounds and geometrical parameters and x corresponds to the in-plane distance to the geometrical center of the circular domains. For simplicity, we ignore the effects associated with the spatial variations of k_o. The external force density (S56) is oriented towards the center of the circular domains, which in this section corresponds to the x direction. Furthermore, we consider $k_o > 0$ because in our experiments the elastic pillars bend towards the center.

Assuming that the deflections of the slender rod are small, the beam theory states that the bending moment $\mathcal{M}(z)$ normal to the $x-z$ plane at position z obeys the relation, Ref. [9, 10],

$$\mathcal{M}(z) = EI\partial_{zz}x, \tag{S57}$$

where E is the Young's modulus of the elastic pillar and I is the geometrical moment of inertia of the elastic pillar's cross-section. For a circular shape the moment of inertia is related to the radius by $I = \pi\delta^4/4$. In the presence of the external force given by Eq. (S56), the equilibrium equation

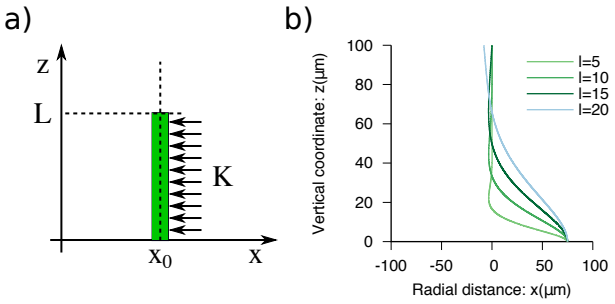

Supplementary figure 4: Steady-state profiles patterns of a slender rod of length subjected to a uniform external force. a) Schematic of the geometry of the system. x represents the spatial coordinate in the direction defined by the geometrical center of a circular island and the center of the elastic pillar. The radial position of the pillar is x_0 and its height at rest L. z corresponds to the vertical coordinate. b) Equilibrium profiles of the shape of a slender rod of length that is subjected to a uniform external force (S56). The equilibrium solutions are given by Eq. (S59) with $L = 100\ \mu m$ and $x_0 = 75\ \mu m$. The values of the length-scale ℓ are indicated in the legend in μm.

for our slender rod, Ref. [9, 10], reads

$$\partial_{zz}\mathcal{M}(z) = -k_o x(z). \tag{S58}$$

The ratio between EI and k_o defines a length scale ℓ given by $\ell = (EI/k_o)^{1/4}$. To determine the profile $x(z)$ from Eq. (S58), we need four boundary conditions. Because the rod is clamped to the substrate, we impose $x(z=0) = x_0$ and $\partial_z x(z=0) = 0$. In addition, we consider that the other end is free, meaning that there is no moment or force. This gives the conditions $\partial_{zz}x(z=L) = 0$ and $\partial_{zzz}x(z=L) = 0$. The equilibrium profile $x(z)$ that is compatible with the previous boundary conditions takes the form

$$\begin{aligned} x(z) = & \frac{x_0(\cosh(z')\cos(L'-z') + (\cosh(L'-z') + 2\cosh(z'))\cos(z'))}{(2+\cos(L')+\cosh(L'))} \\ & + \frac{x_0(\sinh(L'-z')\sin(z') - \sinh(z')\sin(L'-z'))}{(2+\cos(L')+\cosh(L'))} \end{aligned} \tag{S59}$$

where $z' = z/(\sqrt{2}\ell)$, $L' = \sqrt{2}L/\ell$. Supplementary figure 4b shows equilibrium profiles for varying values of ℓ and with a fixed $L = 100\ \mu m$ and $x_0 = 75\ \mu m$. Although Eq. (S59) only provides a good quantitative approximation for small deflections of the slender rod, it is in qualitative agreement with our experimental observations on the shapes of elastic pillars that are clamped away from the geometrical center of the circular domains and inside multicellular mounds.

7.1: Approximation of the net force exerted on an elastic pillar by an aster at steady state

In this subsection, we express in terms of the stress pattern the net force generated by an aster topological defect on an elastic pillar that is placed away from the geometrical center of the circular domain.

For simplicity, we ignore the effects associated with the spatial variations of the physical fields along the direction perpendicular to the substrate plane, and thus we restrict the next analysis to a single plane parallel to the substrate. Besides, we neglect deviations from the stress profiles that are caused by the finite radius of pillars δ.

The parametrization of the elastic pillar interface is given by $\mathbf{r} = (x_0 + \delta\cos(\phi))\hat{x} + \delta\sin(\phi)\hat{y}$, where x_0 corresponds to the position on the x-axis of the geometrical center of the elastic pillar, δ is the pillar radius, ϕ is the parametrization variable that varies from 0 and 2π and $(\hat{x}, \hat{y})$ are the cartesian unit vectors. The unit tangent to the elastic interface is given by $\hat{\mathbf{t}} = \partial_\phi\mathbf{r}/|\partial_\phi\mathbf{r}| = -\sin(\phi)\hat{x} + \cos(\phi)\hat{y}$, where $\partial_\phi\mathbf{r} = -\delta\sin(\phi)\hat{x} + \delta\cos(\phi)\hat{y}$, and the unit normal given by $\hat{\mathbf{n}} = \cos(\phi)\hat{x} + \sin(\phi)\hat{y}$. By relating the previous parametrization to the polar coordinates, we find that the radial coordinate r and the azimuthal angle θ satisfy the relations,

$$r^2 = (x_0 + \delta\cos(\phi))^2 + (\delta\sin(\phi))^2 \tag{S60}$$

$$\cos(\theta) = \frac{x_0 + \delta\cos(\phi)}{\sqrt{(x_0 + \delta\cos(\phi))^2 + (\delta\sin(\phi))^2}} \tag{S61}$$

$$\sin(\theta) = \frac{\delta\sin(\phi)}{\sqrt{(x_0 + \delta\cos(\phi))^2 + (\delta\sin(\phi))^2}} \tag{S62}$$

Under the above-mentioned approximations, we consider that the force per unit area $\mathbf{f}_i$ exerted on an elastic pillar reads

$$\mathbf{f}_i(\mathbf{r}) = \sigma^{\mathrm{tot}}(\mathbf{r}) \cdot \hat{\mathbf{n}}. \tag{S63}$$

The force per unit area $\mathbf{f}_i$ includes a contribution in both the normal direction $\hat{\mathbf{n}}$ and the tangential direction $\hat{\mathbf{t}}$.

The expression of the normal to the pillar interface in polar coordinates is

$$\hat{\mathbf{n}} = (\cos(\phi)\cos(\theta) + \sin(\phi)\sin(\theta))\hat{r} + (\sin(\phi)\cos(\theta) - \cos(\phi)\sin(\theta))\hat{\theta}, \tag{S64}$$

where $\hat{r} = (\cos(\theta), \sin(\theta))$ is the unit vector in the radial direction and $\hat{\theta} = (-\sin(\theta), \cos(\theta))$ is the unit vector in the azimuthal direction. Using the previous expression, we can rewrite Eq. (S63) as

$$\mathbf{f}_i(\mathbf{r}) = \sigma_{rr}^{tot}(\mathbf{r})(\cos(\phi)\cos(\theta) + \sin(\phi)\sin(\theta))\hat{r} + \sigma_{\theta\theta}^{tot}(\mathbf{r})(\sin(\phi)\cos(\theta) - \cos(\phi)\sin(\theta))\hat{\theta}, \tag{S65}$$

where we have assumed that $\sigma^{tot}_{r\theta} = \sigma^{tot}_{\theta r} = 0$, as it is the case for the steady-state stress patterns generated by aster topological defects, see Section IV in Ref. [1].

Using Eqs. (S60)-(S62) and the definitions of the radial $\hat{r}$ and azimuthal $\hat{\theta}$, we can express Eq. (S65) in the cartesian base, as

$$\begin{aligned}\mathbf{f}_i(\mathbf{r}) = &\left(\sigma^{tot}_{rr}(\mathbf{r})(x_0\cos(\phi)+\delta)(x_0+\delta\cos(\phi)) - \sigma^{tot}_{\theta\theta}(\mathbf{r})(x_0\sin(\phi))(\delta\sin(\phi))\right)\frac{\hat{x}}{r^2}\\ &+\left(\sigma^{tot}_{rr}(\mathbf{r})(x_0\cos(\phi)+\delta)(\delta\sin(\phi)) + \sigma^{tot}_{\theta\theta}(\mathbf{r})(x_0\sin(\phi))(x_0+\delta\cos(\phi))\right)\frac{\hat{y}}{r^2},\end{aligned} \tag{S66}$$

where r is given by Eq. (S60).

Using the relation between the normal $\hat{n}$ and the tangential $\hat{t}$ unit vector to the pillar interface and the cartesian base, we can identify both the normal $f_{i,n} = \mathbf{f}_i \cdot \hat{n}$ and tangential $f_{i,t} = \mathbf{f}_i \cdot \hat{t}$ components of the force per unit area $\mathbf{f}_i$ by recasting Eq. (S66) as

$$f_{i,n}(\mathbf{r}) = \frac{\sigma^{tot}_{rr}(\mathbf{r})(x_0\cos(\phi)+\delta)^2 + \sigma^{tot}_{\theta\theta}(\mathbf{r})(x_0\sin(\phi))^2}{r^2} \tag{S67}$$

$$f_{i,t}(\mathbf{r}) = \frac{(\sigma^{tot}_{\theta\theta}(\mathbf{r}) - \sigma^{tot}_{rr}(\mathbf{r}))(x_0\cos(\phi)+\delta)x_0\sin(\phi)}{r^2}, \tag{S68}$$

where we used that $\hat{x} = \cos(\phi)\hat{n} - \sin(\phi)\hat{t}$ and $\hat{y} = \sin(\phi)\hat{n} + \cos(\phi)\hat{t}$. Notably, defining the trace of the total stress $\sigma = (\sigma^{tot}_{rr} + \sigma^{tot}_{\theta\theta})/2$ and the difference $\Delta\sigma = (\sigma^{tot}_{rr} - \sigma^{tot}_{\theta\theta})/2$, one can simplify the previous equations as

$$f_{i,n}(\mathbf{r}) = \sigma(\mathbf{r}) + \frac{\Delta\sigma(\mathbf{r})((x_0\cos(\phi)+\delta)^2 - (x_0\sin(\phi))^2)}{(x_0+\delta\cos(\phi))^2 + (\delta\sin(\phi))^2} \tag{S69}$$

$$f_{i,t}(\mathbf{r}) = \frac{-2\Delta\sigma(\mathbf{r})(x_0\cos(\phi)+\delta)x_0\sin(\phi)}{(x_0+\delta\cos(\phi))^2 + (\delta\sin(\phi))^2}, \tag{S70}$$

The net force per unit length on the elastic pillars corresponds to

$$F_i = \int \mathbf{f}_i(\mathbf{r})\delta d\phi. \tag{S71}$$

To linear order in $\epsilon = \delta/x_0 \ll 1$, the contribution to the net force of the normal forces to the pillar interface is found to be

$$F_{i,n} = \int \mathbf{f}_{i,n}(\mathbf{r})\hat{n}\delta d\phi \approx \frac{\pi\delta^2}{2x_0}\left(2\Delta\sigma + x_0(\partial_r\Delta\sigma + 2\partial_r\sigma)\right)|_{r=x_0}\hat{x} \tag{S72}$$

Likewise, the contribution to the net force of the tangential forces to the pillar interface up to linear order in $\epsilon = \delta/x_0 \ll 1$ is found to be

$$F_{i,t} = \int \mathbf{f}_{i,t}(\mathbf{r})\hat{t}\delta d\phi \approx \frac{\pi\delta^2}{2x_0}\left(2\Delta\sigma + x_0\partial_r\Delta\sigma\right)|_{r=x_0}\hat{x}. \tag{S73}$$

Considering the stress components $\sigma = \sigma_0 + \alpha r^2/R^2$ and $\Delta\sigma = \beta r^2/R^2$ scale quadratically with r, as it is the case for the steady-state stress patterns in aster topological defects, Ref. [1], one obtains that the previous equations become

$$F_{i,n} = \frac{2\pi\delta^2}{R^2}\,(\alpha+\beta)\,x_0\hat{x} \tag{S74}$$

$$F_{i,t} = \frac{2\pi\delta^2}{R^2}\,(\beta)\,x_0\hat{x}. \tag{S75}$$

For the specific choice of the stress components made above, the components of the net forces (S74)-(S75) are exact solutions irrespective of the order of ϵ.

In general, the total net force (S71) exerted on an elastic pillar is a linear combination of Eqs. (S74) and (S75) due to asymmetries in the transmission of both tangential and normal forces on the pillar's interface. Both of these force components have an x component that scales linearly with the distance between the pillar's center and the confinement center x_0 and their y component vanishes. These features justify our choice for the external force (S56). The pre-factors α and β may depend on the specific details of the active force generation mechanism or the boundary conditions at the pillar interface. Furthermore, expressions (S74) and (S75) are independent of the constant σ_0, which suggests that this force is independent of mechanisms that give a constant stress like a surface tension.

Here, we have assumed that the stress patterns are unaltered by the presence of an elastic pillar. The deviations of the stress patterns due to the presence of an elastic pillar could introduce corrections to Eqs. (S74)-(S75) of linear order in ϵ. Although these expressions are correct only in the limit, where the diameter of the pillars tends to zero, they give an approximate value for pillars with finite diameter. In particular, we expect that the qualitative features mentioned above remain to linear order in ϵ.

SUPPLEMENTARY NOTE 8: STEADY-STATE MECHANICS OF INTEGER TOPOLOGICAL DEFECTS IN LARGE CONFINING DOMAINS

In this section, we discuss the influence of the boundary on the steady state solutions. To this end, we study the confining domain radius R to be large compared to the characteristic length scale associated with the active polar fluid. Correspondingly, we consider the free energy $\mathcal{F}$ given by Eq. (S31) in Supplementary note 1.6, which is supported by the fact that C2C12 myoblasts form long-ranged orientational order patterns in large confining domains, Ref. [6]. However, the results of this section show that this situation is not appropriate for describing our experiments.

We consider that the equilibrium value of the polar order parameter $S_{eq} = \sqrt{\chi_2/\chi_4} = 1$, which is equal to the order at the boundary of the circular domain that we impose in the main text and Supplementary notes 2 and 4. Additionally, we set the lengthscale to be $\sqrt{\mathcal{K}/\chi_2} = 1$, which is related to the size of the disordered domain around the topological defect center.

We focus on integer topological defects with $\psi = \psi_0 = const$, such that $h_\perp = 0$, Eq. (S40). where asters correspond to $\psi_0 = 0$, spirals to $0 < \psi_0 < \pi/2$, and vortices to $\psi_0 = \pi/2$. For $\psi_0 = 0$, Eq. (S11) is satisfied, because $v_{r\theta} = 0$ due to the symmetries of asters. In the general case, Eq. (S11) implies $\nu \cos(2\psi_0) = 1$. This conditions requires that $|\nu| \geq 1$ for a real solution of ψ_0. The steady-state profile of the polar order parameter S is in general determined by Eq. (S10), which shows that shear flows can generate long-ranged orientational order. In this section, we neglect this possibility and limit our discussion to the case where $|\gamma\nu \sin(2\psi_0) v_{r\theta}| \ll h_\parallel$. In this situation, flow alignement does essentially not contribute to the polar order S and according to Eq. (S10), we have $h_\parallel \approx 0$. Instead the steady state profile of S is set by Eq. (S39) with boundary conditions (S19)-(S20) for both asters and spirals. Supplementary figure 5a shows the steady-state profiles of $S(r)$ for different radii R.

Using the previous approximations, the components of the deviatory stress for spirals read

$$\sigma_{rr,\theta\theta} \approx \mp\frac{1}{2} S^2 \cos(2\psi_0)\zeta\Delta\mu - S^2\zeta''\Delta\mu \tag{S76}$$

$$\sigma_{r\theta,\theta r} \approx 2\eta v_{r\theta} - \frac{1}{2} S^2 \sin(2\psi_0)\zeta\Delta\mu. \tag{S77}$$

Furthermore, the force balance equations (S14) and (S18) simplify to

$$\partial_r \left(\frac{B(n-n_0)}{n_0} \right) \approx T_0 S\cos(\psi_0) - \zeta\Delta\mu\cos(2\psi_0)\left(\frac{S^2}{r} + S\partial_r S\right) - \zeta''\Delta\mu 2S\partial_r S \tag{S78}$$

$$\eta\left(\partial_{rr} v_\theta + \frac{\partial_r v_\theta}{r} - \frac{v_\theta}{r^2}\right) - \xi v_\theta \approx -T_0 S\sin(\psi_0) + \zeta\Delta\mu\sin(2\psi_0)\left(\frac{S^2}{r} + S\partial_r S\right) \tag{S79}$$

where for simplicity, we considered the limit of small deviations of the cell number density n with respect to the reference value n_0. We can define the friction length $\lambda = \sqrt{\eta/\xi}$.

Next, we study the dependence on the confinement radius R of the steady-state cell number density n and azimuthal velocity v_θ profiles. Equation (S78) shows the cell number density patterns n generated by three different active processes, namely, gradients of the anisotropic and isotropic active stresses, which are proportional to $\zeta\Delta\mu$ and $\zeta''\Delta\mu$ respectively, and traction forces, which are proportional to T_0. The azimuthal velocity v_θ is generated by the anisotropic stress and the traction forces (S79). Because these equations are linear in n and v_θ, we computed numerically their steady-state profiles for each of the three different active processes separately for different

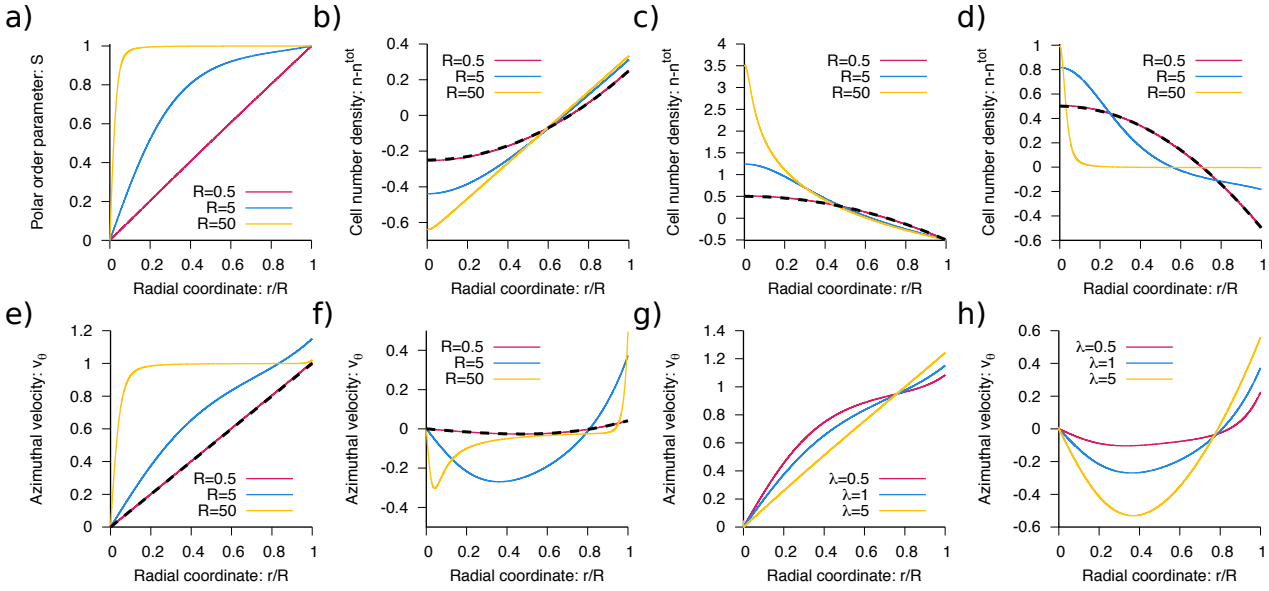

Supplementary figure 5: Steady-state patterns around integer topological defects for varying confining radius R and parameter λ. a) Polar order parameter S, b-d) cell number density $n - n^{\rm tot}$ and e-h) azimuthal velocity v_θ profiles at steady state. The density scale in panel b) is $n_0 T_0 R S_{eq} \cos(\psi_0)/B$, in c) is $n_0 \zeta \Delta\mu \cos(2\psi_0) S_{eq}^2/B$ and in d) is $n_0 \zeta'' \Delta\mu S_{eq}^2/B$. The velocity scale in panels e and g) is $T_0 S_{eq} \sin(\psi_0)/\xi$ and in panels f and h) is $\zeta \Delta\mu \sin(2\psi_0) S_{eq}^2 \sqrt{\mathcal{K}/\chi_2}/\eta$. In panels (a-d), the values of R are in the legend; in panels (e-f), the values of R are in the legend and $\lambda = \sqrt{\eta/\xi} = 1$; in panels (g-h) the values of λ are in the legend and $R = 5$. The black dashed curves in panel b-d) correspond to Eq. (60) in Ref. [1] for each of the three different active processes and in the limit $\gamma \tan(2\psi_0)^2/4\eta \to 0$. The black dashed curves in panels e) and f) correspond to Eq. (43) and (48) in Ref. [1].

confining radii R. Supplementary figure 5b-h shows that for a broad range of radii R, the cell number density and the azimuthal velocity profiles are qualitatively similar to the steady state profiles in the limit of small domains, $R \ll 1$. Quantitative differences are found in the profiles of the previous physical variables for varying radius R, Supplementary figure 5b-h. For a fixed radius $R = 5$ and varying friction length $\lambda = \sqrt{\eta/\xi}$, we found that in the case the azimuthal velocity profiles are generated by the active anisotropic stresses decay from the boundary over a length scale controlled by the friction length $\lambda = \sqrt{\eta/\xi}$, Supplementary figure 5h. This feature was also reported in the limit of small confining domains [1]. Altogether, these results show that qualitative features of the mechanical patterns around the center of integer topological defects, such as cell number density and azimuthal velocity profiles in both aster and spirals, are independent of the presence of a confining domain.

SUPPLEMENTARY REFERENCES

* These authors contributed equally to this work

† Electronic address: karsten.kruse@unige.ch

‡ Electronic address: aurelien.roux@unige.ch

[1] C. Blanch-Mercader, P. Guillamat, A. Roux, and K. Kruse, Phys. Rev. E **103**, 012405 (2021).

[2] K. Kruse, J. F. Joanny, F. Jülicher, and J. Prost, Phys. Biol. **3**, 130 (2006).

[3] S. R. de Groot and P. Mazur. Non-Equilibrium Thermodynamics. Dover Publications Inc, New York (1985).

[4] J. F. Joanny, F. Jülicher, K. Kruse, and J. Prost, New J. Phys. **9**, 422 (2007).

[5] S. Fürthauer, M. Neef, S. W. Grill, K. Kruse, and F. Jülicher, New J. Phys. **14**, 023001 (2012).

[6] G. Duclos, S. Garcia, H. G. Yevick, and P. Silberzan, Soft Matter **10**, 2346 (2014).

[7] J. L. Ericksen, Arch. Ration. Mech. Anal. **9**, 371 (1962).

[8] P. G. de Gennes and J. Prost, *The Physics of Liquid Crystals*, 2nd ed., International Series of Monographs on Physics (Oxford University Press, Oxford, 2002).

[9] V. Bormuth, J. Barral, J.-F. Joanny, F. Jülicher, and P. Martin, Proc. Natl. Acad. Sci. U. S. A. **111**, 7185 (2014).

[10] L. D. Landau and E. M. Lifshitz, *Theory of Elasticity*, 3rd ed., (Pergamon, New York, 1986).